Rare Metal Materials and Engineering
Volume 54, Issue 4, April 2025
Available online at www.rmme.ac.cn

Science Press

Cite this article as: Yang Jinlong, Xiong Jiangying, Yin Chao, et al. Influence of Microstructures on Hot Deformation Behavior and Microstructure Evolution of FGH4113A Superalloy[J]. Rare Metal Materials and Engineering, 2025, 54(04): 898-907. DOI: https://doi.org/10.12442/j.issn.1002-185X.20240199.

ARTICLE

Influence of Microstructures on Hot Deformation Behavior and Microstructure Evolution of FGH4113A Superalloy

Yang Jinlong[1,2], Xiong Jiangying[2,3], Yin Chao[3], Cheng Junyi[2,3], Guo Jianzheng[2,3], Feng Ganjiang[2,3]

[1] Shenzhen Wedge Aviation Technology Co., Ltd, Shenzhen 518000, China; [2] Powder Metallurgy Research Institute, Central South University, Changsha 410083, China; [3] Shenzhen Wedge Central South Research Institute Co., Ltd, Shenzhen 518000, China

Abstract: The hot compression curves and deformed microstructures were investigated under various hot deformation conditions in three states: hot isostatic pressing (HIP, A1), HIP+hot extrusion at 1100 ℃ (A2), and HIP+hot extrusion at 1150 ℃ (A3). The results show that A2 sample, extruded at 1100 ℃ with uniform $\gamma+\gamma'$ duplex microstructures, demonstrates excellent hot deformation behavior at both 1050 and 1100 ℃. The true stress-true strain curves of A2 sample maintain a hardening-softening equilibrium over a larger strain range, with post-deformation average grain size of 5 μm. The as-HIPed A1 sample and 1150 ℃ extruded A3 sample exhibit a softening region in deformation curves at 1050 ℃, and the grain microstructures reflect an incomplete recrystallized state, i. e. combination of fine recrystallized grains and initial larger grains, characterized by a necklace-like microstructure. The predominant recrystallization mechanism for these samples is strain-induced boundary migration. At 1150 ℃ with a strain rate of 0.001 s^{-1}, the influence of the initial microstructure on hot deformation behavior and resultant microstructure is relatively less pronounced, and post-deformation microstructures are fully recrystallized grains. Fine-grained microstructures are conducive to maximizing the hot deformation potential of alloy. By judiciously adjusting deformation regimes, a fine and uniform deformed microstructure can be obtained.

Key words: FGH4113A superalloy; initial microstructure; hot deformation behavior; microstructure evolution

1 Introduction

Nickel-based powder metallurgy (PM) superalloys exhibit excellent comprehensive properties, high-temperature microstructural stability and uniformity, making them appropriate for advanced aviation engine turbine disks[1]. The thermal deformation process of nickel-based PM superalloys usually involves hot isostatic pressing (HIP), hot extrusion (HEX), and isothermal forging. The microstructures are greatly influenced by forming processes. For instance, the microstructure after HIP may exhibit uneven grain sizes, potential presence of prior particle boundary (PPB) and larger-sized residual γ' phase after cooling. The HIP microstructures are related to powder particle size, surface adsorption, segregating elements, and the HIP process itself[2–4]. The extrusion process can break up the PPBs left from the HIP state, typically resulting in a $\gamma+\gamma'$ duplex microstructure that provides suitable microstructure conditions and billets for forging. The differences in extrusion microstructure are related to the extrusion process and the initial HIP micro-structures[5–7]. To harness the alloy ' s optimal performance and desired microstructure, it is crucial to delve into the influence of different initial microstructures on thermal deformation and microstructure evolution. Additionally, a comprehensive study on the evolutionary trends during the thermal deformation process is paramount for refining the microstructures.

Thermal compression tests have been commonly used in several studies to investigate the hot deformation behavior and microstructure evolution of superalloy[8–22]. For the as-HIPed FGH96 alloy, γ' phase exists after deformation at 1050 ℃, and

Received date: April 03, 2024
Foundation item: Shenzhen Science and Technology Program (KJZD20230923113900001); Project of Industry and Information Technology Bureau of Shenzhen Municipality (201806071403422960)
Corresponding author: Guo Jianzheng, Ph. D., Professor, Powder Metallurgy Research Institute, Central South University, Changsha 410083, P. R. China, Tel: 0086-755-82799834, E-mail: 948087455@qq.com

fine recrystallized grains are extensively distributed along the initial grain boundaries. Complete dynamic recrystallization (RX) is achieved at 1140 ℃[8]. During hot deformation, dynamic RX nucleation sites include the PPB location, regions with critical dislocation density accumulation, recrystallized grain boundaries containing deformation dislocation and twin boundaries[9]. For the extruded FGH96, continuous dynamic recrystallization (CDRX) and discontinuous dynamic recrystallization (DDRX) occur at low-temperature deformation condition, while only DDRX takes place after high-temperature deformation[10]. For as-HIPed and deformed fine grains of the superalloy FGH4096, the fine-grained alloy has a higher flow stress at 1050 ℃ than the as-HIPed alloy, but the as-HIPed alloy has a higher flow stress in the 1080–1140 ℃ range[11]. Samples with smaller initial grain sizes have a higher proportion of grain boundaries, increasing the chances of RX nucleation and facilitating rapid dynamic RX[16]. Delving into the U720Li superalloy, comprehensive research has been conducted on its thermal compression deformation behavior and microstructural evolution[19–22]. Detailed studies on RX dynamics within the $\gamma+\gamma'$ duplex and γ phase regions[20] reveal that the intrinsic γ' phase within grains significantly impedes dislocation slip, thereby inhibiting the formation of high-density dislocation substructures and sub-grain. Another study focusing on the fine-grained $\gamma+\gamma'$ duplex region of U720Li highlighted localized grain boundary slippage and strain-induced RX as the principal deformation mechanisms[21]. Collating insights from these studies, the focal point of thermal deformation research gravitates towards γ' phase and RX dynamics. Here, the γ' phase plays a dual role, simultaneously acting as a barrier and catalyst to deformation behavior, while the RX process is intimately intertwined with γ' phase and thermal deformation parameters.

The FGH4113A alloy represents an innovative nickel-based PM superalloy, demonstrating exceptional operational capabilities at temperature up to 800 ℃. Depending on its processing, whether through HIP or HEX, the initial microstructures are different. Notably, with increasing the extrusion temperature, the microstructure showcases larger grain sizes and fewer coarse γ' phases. After HIP, the dominant microstructural features are coarse γ' phases interspersed with sporadic PPBs. These initial states, with their inherent microstructural characteristics, significantly influence the alloy's subsequent hot deformation behavior. Therefore, elucidating the relationship between deformation-induced stress-strain curves, initial microstructure, and microstructural variations is extremely important. This study aims to unravel the multifaceted influences of initial microstructures on the hot deformation behavior and microstructure evolution of FGH4113A alloy by thermal compression tests. In addition, the influence of γ' phase on microstructure evolution and its dissolve was investigated.

2 Experiment

2.1 Materials

The nominal composition of superalloy FGH4113A is outlined in Table 1. This PM superalloy was fabricated by the following steps, as shown in Fig. 1. Firstly, the powder was prepared via argon atomization, subsequently sieved through a 270-mesh screen, and then encapsulated within an AISI 304 stainless steel capsule. After vacuum degassing, the capsule was densified by HIP treatment at 1150 ℃ for 4 h under a pressure of 150 MPa. The HIP device was AIP20-96-30H. The HIP component was 240 mm in diameter and 270 mm in height. Thereafter, the HIP material was shaped into bars using a 5000 t vertical extruder, with an extrusion ratio of 4.5, speeds ranging from 20 mm/s to 35 mm/s, and temperature of 1100 (sub-solvus temperature) and 1150 ℃ (sup-solvus temperature). The extrusion bar was 100 mm in diameter and 1150 mm in length. The HIP parts and extruded bars were prepared by Shenzhen Wedge Central South Research Institute Co., Ltd.

2.2 Hot compression

A Gleeble 3180 thermo-simulation machine was utilized to conduct hot compression tests. Specimens with 8 mm in diameter and 12 mm in height were wire-cut from the extruded bars. The direction of deformation was axial, with a total deformation translating to about a 50% height reduction,

Table 1 Nominal composition of FGH4113A alloy (wt%)

Co	Cr	Al	Ti	Ta	W	Mo	Nb	C, Hf, B and Zr	Ni
19.0	13.0	3.0	3.7	1.0	4.0	4.0	1.2	Minor	Bal.

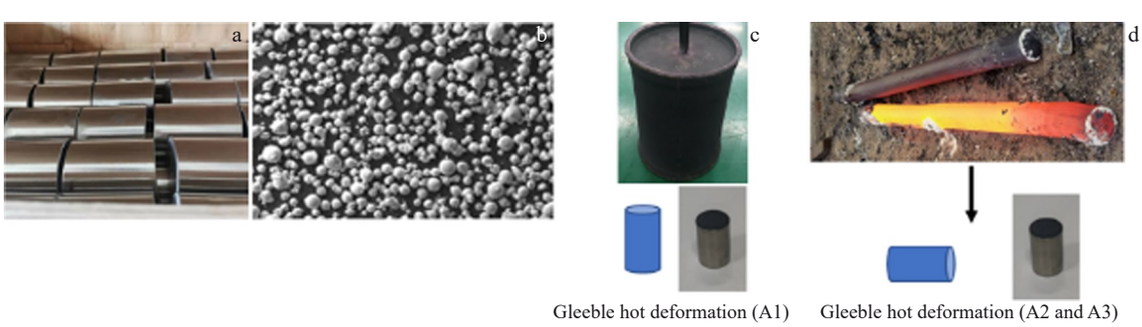

Fig.1 Preparation process of hot compression sample: (a) alloy ingot, (b) argon atmosphere powder, (c) HIP part, and (d) hot extruded bars

equating to a true strain of 0.69. A consistent heating rate of 5 ℃/s was maintained, and a soaking duration of 3 min at the deformation temperature ensured microstructural uniformity prior to the compression test. After compression, the samples were subjected to argon cooling to retain their microstructures. Concurrently, an automated data acquisition system captured the true stress-strain data throughout the hot deformation process.

2.3 Microstructure observation

The samples for initial microstructure observation were sourced from the HIP part (A1) and extruded bars (hot extruded at 1100 and 1150 ℃, marked as A2 and A3, respectively). The samples were cube with 10 mm in size.

Each compressed specimen was sectioned centrally and in alignment with the compression axis. In-depth microstructural analyses were conducted using both the NikonMM~400 optical microscope (OM) and the Sigma300 scanning electron microscope (SEM) equipped with electron back scattered diffraction (EBSD). Prior to observation, the samples were ground, polished, and chemically etched via a solution comprising HNO_3, H_2O, CH_3COOH, and HF in a volume ratio of 3:3:3:1. Depending on the grain size, EBSD mapping was facilitated with a step size between 0.1 and 1.0 μm. Grains were characterized by a cluster more than 10 pixels with a misorientation below 10°. A grain orientation spread (GOS) threshold of 2° was set to identify the recrystallized grains[23–24].

For TEM analysis, samples were firstly ground to a thickness from 50 μm to 70 μm, followed by punching to produce standard disks with 3 mm in diameter. These disks were further thinned via electrolysis using an electrolyte composed of 10% $HClO_4$ and 90% CH_3CH_2OH at approximately –25 ℃. Subsequent cleaning was performed using ion-milling, with the sample tilted at an angle of 2° at 3 kV for a span of 10 min.

3 Results and Discussion

A1 sample was subjected to HIP at 1150 ℃, followed by furnace cooling. As shown in Fig. 2, the initial microstructure of A1 sample exhibits a substantial presence of PPB and large primary γ' phase. The size of the primary γ' phase remains <2 μm, scattered randomly within the γ matrix and at grain boundaries. Moreover, a significant quantity of secondary γ' phases appears, exhibiting irregular shapes. At extrusion temperature of 1100 ℃, the microstructure of A2 is a $\gamma'+\gamma$ dual-phase and contains numerous large γ' phase, each within 2 μm. Conversely, the A3 sample, extruded at 1150 ℃, has some large grains with most γ' phase dissolved and fewer coarse and intergranular γ' phase. The average grain sizes of A1, A2, and A3 samples are around 6.7, 3.7, and 8.7 μm, respectively. The GOS results in Fig. 2a–2c indicate that microstructures are fully recrystallized grains. Differences in grain size and grain boundary orientation exist among samples. The grain boundary impacts the metal's plastic deformation by dislocation nucleation sites and impediments to dislocation movement[16,22,25].

The true stress-true strain curves for samples under different deformation conditions are presented in Fig. 3. To study the deformed and recrystallized microstructure, hot compression deformation at 1050 ℃ was employed. During deformation at 1050 ℃, true stress-true strain curve of A2 sample easily attained a balanced state. At 1050 ℃-0.01 s^{-1}, the stress-strain curves of A1 and A3 samples present similar characteristics, under-going a sequence hardening followed by softening as strain accumulates. Conversely, A2 sample exhibits a distinct hardening-softening equilibrium (Fig. 3a). At 1050 ℃-0.001 s^{-1}, A1 and A2 samples have comparable deformation characteristics, distinctly demonstrating a hardening-softening equilibrium, whereas the A3 sample's curves resemble that observed at 1050 ℃-0.01 s^{-1}, with a reduced peak stress (Fig. 3b). Work-hardening in the alloy

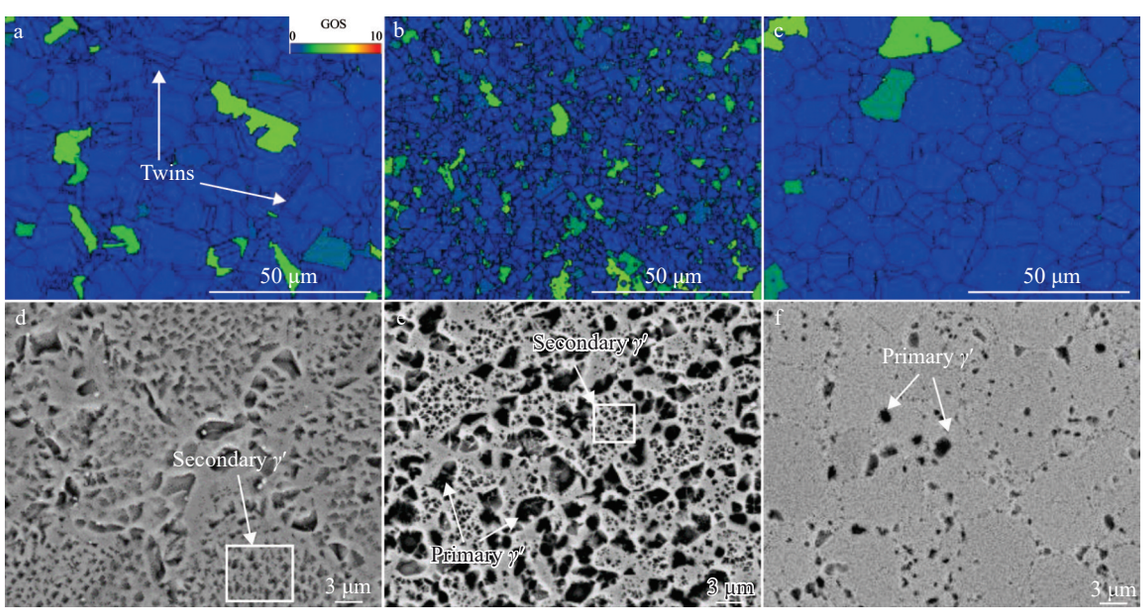

Fig.2 GOS (a–c) and SEM images of samples under different initial conditions: (a, d) A1, (b, e) A2, and (c, f) A3

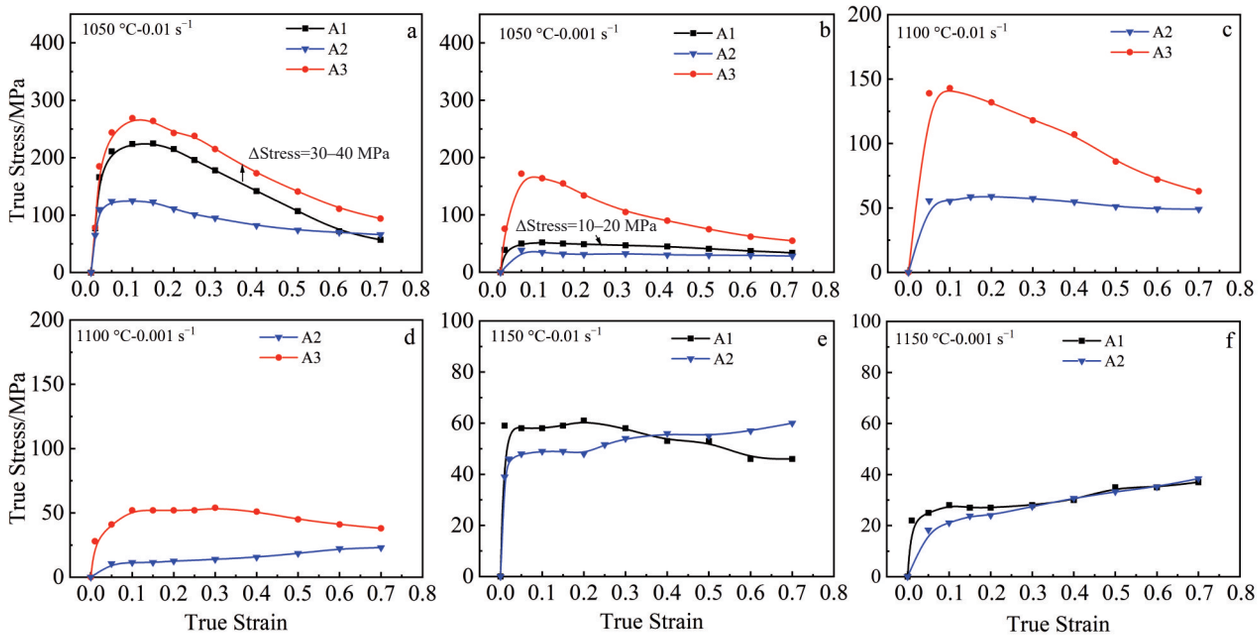

Fig.3 True stress-true strain curves of samples under different deformation conditions: (a) 1050 °C-0.01 s^{-1}, (b) 1050 °C-0.001 s^{-1}, (c) 1100 °C-0.01 s^{-1}, (d) 1100 °C-0.001 s^{-1}, (e) 1150 °C-0.01 s^{-1}, and (f) 1150 °C-0.001 s^{-1}

arises from dislocation multiplication, while softening primarily stems from dynamic RX, which consumes deformed grains and forms grains free from deformation dislocations[22]. A hardening-softening equilibrium indicates a balance between dislocation multiplication hardening and dynamic RX softening.

The typical forging temperature range for extruded samples is 1050–1100 °C[26–27]. A2 and A3 samples were subjected to hot compression tests at 1100 °C under strain rates of 0.01 and 0.001 s^{-1}, as depicted in Fig.3c and 3d, respectively. At strain rate of 0.001 s^{-1}, A2 sample manifests a hardening-softening balance within the strain range of 0.1–0.7, while A3 sample displays gradual softening over the same range. At strain rate of 0.01 s^{-1}, both A2 and A3 samples predominantly show a hardening-softening equilibrium over a wide strain range. Notably, A2 sample undergoes secondary hardening beyond a strain of 0.5, indicating the thorough RX in the alloy and subsequent deformation of recrystallized grains.

Hot compression tests were conducted on A1 and A2 samples at a high temperature of 1150 °C with strain rates of 0.01 and 0.001 s^{-1}. Following a hardening-softening equilibrium, A1 sample exhibits partial softening when the strain reaches 0.4, while A2 sample demonstrates secondary hardening. At strain rate of 0.001 s^{-1}, the stress-strain curves for both states of samples are similar, consistently indicating progressive secondary hardening.

The SEM images and grain boundary of the samples deformed at 1050 °C under strain rates of 0.01 and 0.001 s^{-1} are illustrated in Fig.4. Compared to A2, A1 sample retains a larger quantity of secondary γ' phases, while its primary γ' phases are smaller in size and fewer in number. The SEM morphologies of A1 sample under both strain rates are similar. However, A3 sample retains primary γ' phases at the grain boundaries and exhibits an increased presence of fine secondary γ' phases. Compared to their initial HIP and HEX states, the content of primary γ' phase decreases after deformation at 1050 °C. During hot compression process, the morphology of γ' phase changes from cauliflower-like and irregular shapes to spherical forms. The interfacial energy and lattice misfit lead to the spheroidization of γ' phase. Meanwhile, the interaction between dislocation and γ' phase also promotes the spheroidization of γ' phase[28–29].

When comparing fractions of low-angle grain boundary (LAGB, with misorientation angles between 0°–15°, shown in black) and high-angle grain boundary (HAGB, with misorientation angles greater than 15° , shown in red), A2 sample exhibits a larger fraction of HAGB (83.3% at 0.01 s^{-1} and 86% at 0.001 s^{-1}), indicating a more comprehensive RX. In contrast, both A1 and A3 samples have coexisting LAGB and HAGB, displaying a distinct necklace-like microstructure, which indicates insufficient RX[9,22,30–31]. When comparing the two strain rates, the A1 microstructure exhibits a greater presence of twin boundaries.

As shown in Fig.3a, the true stress-true strain curves of A1 and A3 samples are similar, both microstructures of which are incomplete, displaying progressive softening. A comparison between A2 and A3 samples reveals that fine-grained microstructure is beneficial to RX during hot deformation. After deformation at 1050 °C under strain rate of 0.001 s^{-1}, the average grain sizes of A1, A2, and A3 samples are 4.1, 3.6, and 4.4 μm, respectively, while at strain rate of 0.01 s^{-1}, they are 3.7, 3.0, and 4.6 μm, respectively. A1 and A3 samples have larger initial grain sizes.

The RX fraction of fine-grained sample (A2) is higher than that of coarse-grained sample (A1 and A3). Furthermore, as shown in Fig.3a and 3b, a decrease in peak stress is observed

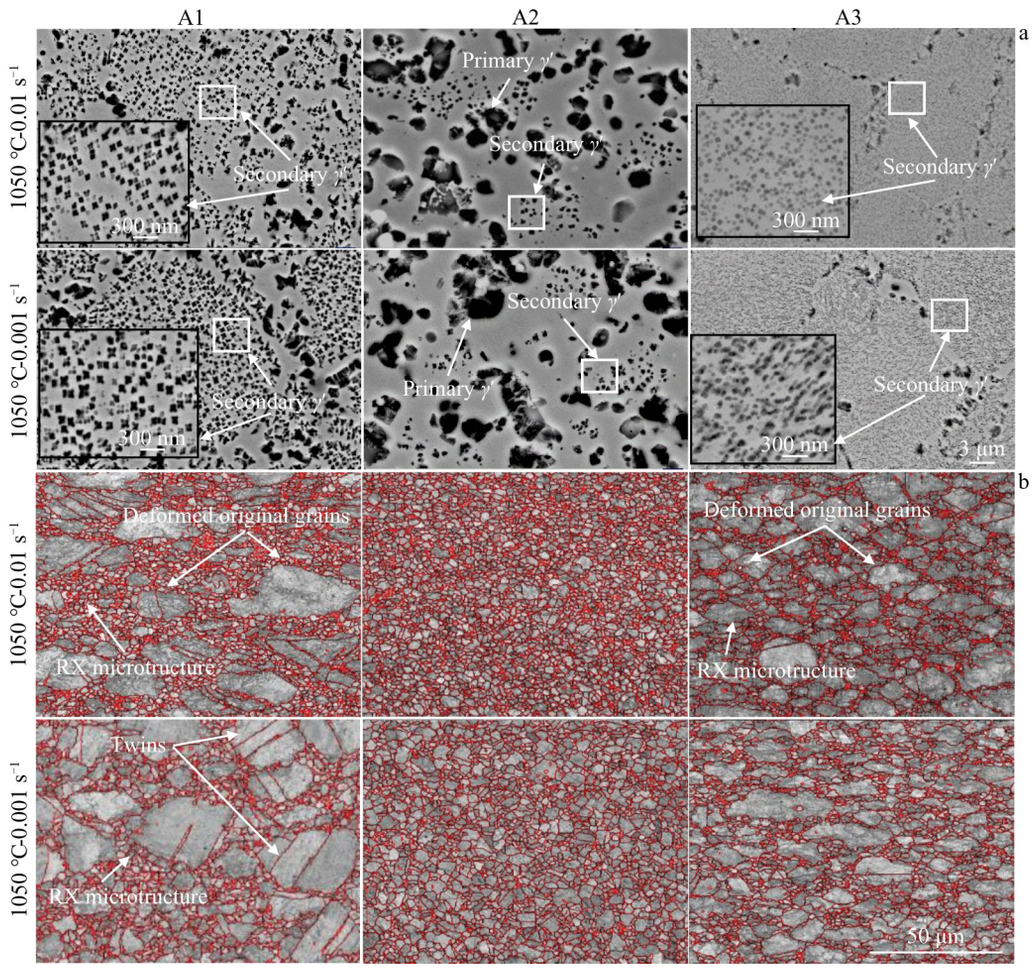

Fig.4 SEM images (a) and grain boundaries (b) of samples after hot deformation at 1050 ℃ with different strain rates

with a decrease in the initial grain size. The RX initiates earlier in fine-grained A2 than in the coarse-grained A1 and A3. This is because fine grains enhance the nucleation associated with the increased grain boundary area per unit volume[16,32–33], and the triple junctions are highly favorable sites for nucleation of RX grain[34]. According to the viewpoints of Li[14] and Yang et al[29], during compression process, the primary γ' phase becomes the nucleation site for RX. Therefore, fine grain and primary γ' phase promotes the RX process in A2 sample.

The microstructures of A2 and A3 samples after deformation at 1100 ℃ with strain rates 0.01 and 0.001 s^{-1} are presented in Fig.5. The grain boundaries in A2 sample consist mainly of HAGB, while the A3 sample exhibits necklace-like microstructure. The fine-grained A2 sample undergoes more comprehensive RX than the coarse-grained A3. For A3 sample, a significant difference is observed between the stress-strain curves at strain rates of 0.01 and 0.001 s^{-1}. The microstructure has more recrystallized grain boundaries and larger grain size at lower strain rate of 0.001 s^{-1} than that at 0.01 s^{-1}. After deformation at 1100 ℃ with strain rate of 0.001 s^{-1}, the average grain sizes for A2 and A3 samples are 3.3 and 3.9 μm, respectively. While at strain rate 0.01 s^{-1}, they are 3.3 and 5.2 μm, respectively. The kernel average misorientation (KAM) value is related to the residual plastic deformation and dislocation density[35–36]. Comparing the distributions under different conditions, the A2 sample consists mainly of recrystallized grains with minimal residual plastic deformation, as reflected by smaller KAM values. In contrast, the initial grains in the A3 sample have a higher residual plastic strain, as reflected by larger KAM values.

The microstructures of A1 and A2 samples after deformation at 1150 ℃ with strain rates of 0.01 and 0.001 s^{-1} are depicted in Fig. 6. When deformed at 1150 ℃ , the influence of the initial microstructure on the deformation process is not evident. The microstructures under all four conditions are characterized by large recrystallized grains, with the majority of γ' phase dissolved back into the matrix. The lager grain sizes are attributed to the loss of the pinning effects of γ' phase. At strain rate of 0.001 s^{-1}, the grain sizes in A1 and A2 samples are noticeably coarser than those at 0.01 s^{-1}. Specifically, after deformation at 1150 ℃-0.001 s^{-1}, the average grain sizes for A1 and A2 samples are 30.7 and 20.5 μm, respectively, whereas at higher strain rate of 0.01 s^{-1}, they are 13.0 and 12.4 μm, respectively. The growth of recrystallized grains is apparently related to the sufficient deformation time at lower strain rates.

The true stress-true strain curves under different strain

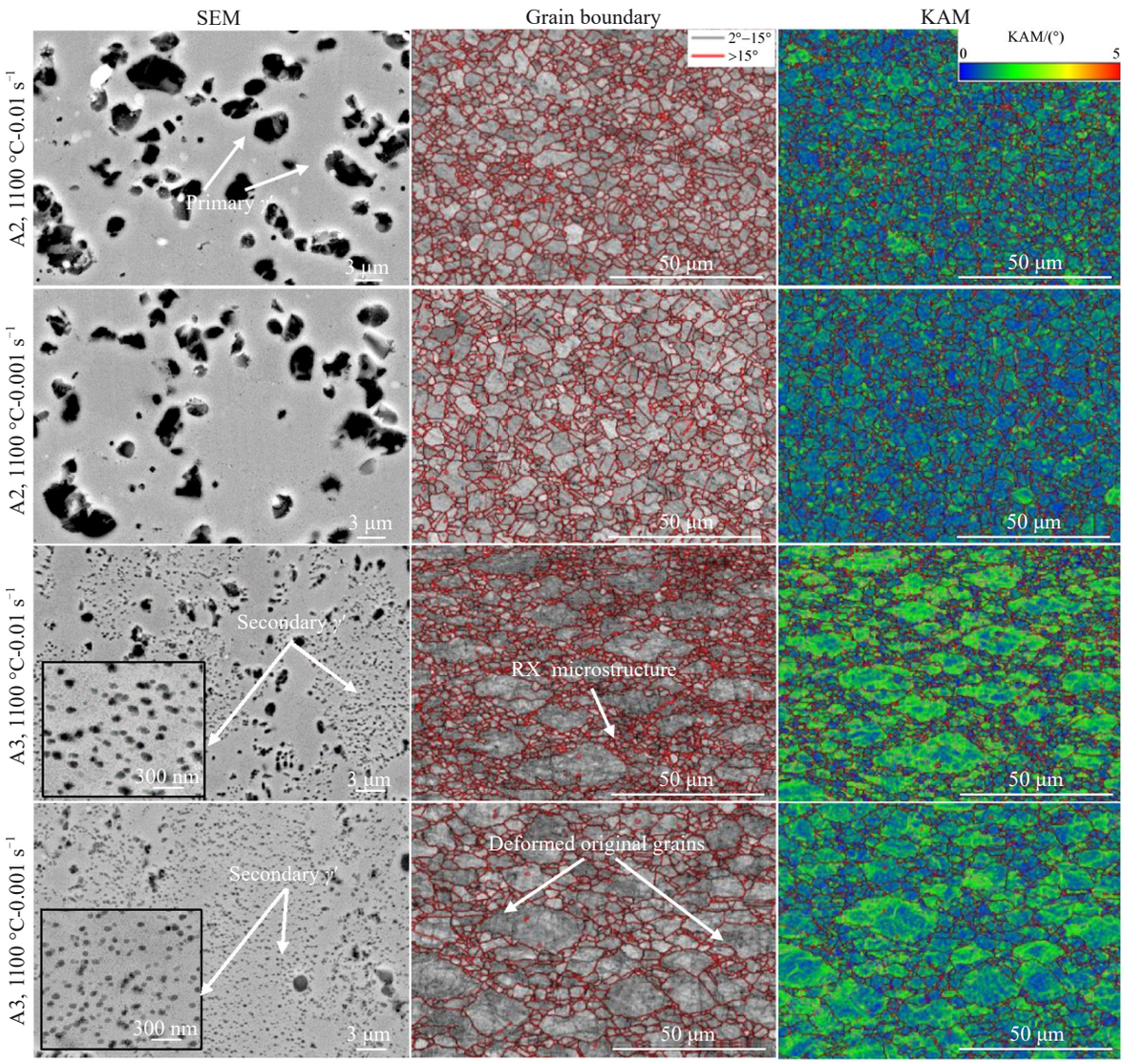

Fig.5 SEM image, grain boundary, and KAM distribution of samples after hot deformation at 1100 ℃ with different strain rates

conditions, as well as the grain size, grain boundary misorientation distribution, GOS, and KAM distribution of the structure after hot deformation, are illustrated in Fig. 7. In the initial microstructure (Fig. 7a), the grain size of the A2 sample is smaller than that of A1 and A3 samples, while the A1 sample exhibits a broader grain size distribution. Comparing the grain boundary misorientation distribution graphs, the A1 sample has a proportion of twin boundary (grain boundary orientation angle at 60°[23–37]). The average value of grain boundary misorientation angles for A3 and A2 samples are similar. In the GOS distribution map, the GOS values for A2 sample are larger than that for A1 and A3 samples, which is consistent with the KAM value distributions.

After deformation at 1050 ℃ with strain rate of 0.01 s^{-1} (Fig. 7b), the GOS and KAM values of A2 sample are smaller, accompanied by a finer average grain size, a narrow distribution, and a larger average grain boundary misorientation angle, indicating that the A2 sample has entered a hardening-softening equilibrium stage. Meanwhile, the stress-strain curves for A1 and A3 samples are similar, both falling into the softening region. The GOS and KAM values are larger, suggesting a higher initial grain content and greater strain accumulation. Compared to A3, A1 sample has a higher proportion of LAGB, twins, and smaller size grains. The lower GOS and KAM values in the A1 sample indicate a higher degree of RX.

After deformation at 1100 ℃ with strain rate of 0.01 s^{-1} (Fig. 7c), the true stress-true strain curve for A2 sample is in a hardening-softening equilibrium state, while the A3 sample gradually softens. The GOS and KAM results reveal that most grains in the A2 sample are recrystallized, whereas A3 sample has more deformed grains, with greater internal plastic accumulation and higher sub-grain and LAGB proportions.

After deformation at 1150 ℃ with strain rate of 0.01 s^{-1} (Fig. 7d), the grain size and grain boundary misorientation angles of A1 and A2 samples are similar. Compared to A1, A2 sample has a higher flow stress and GOS values. The increasing flow stress indicates that some recrystallized grains

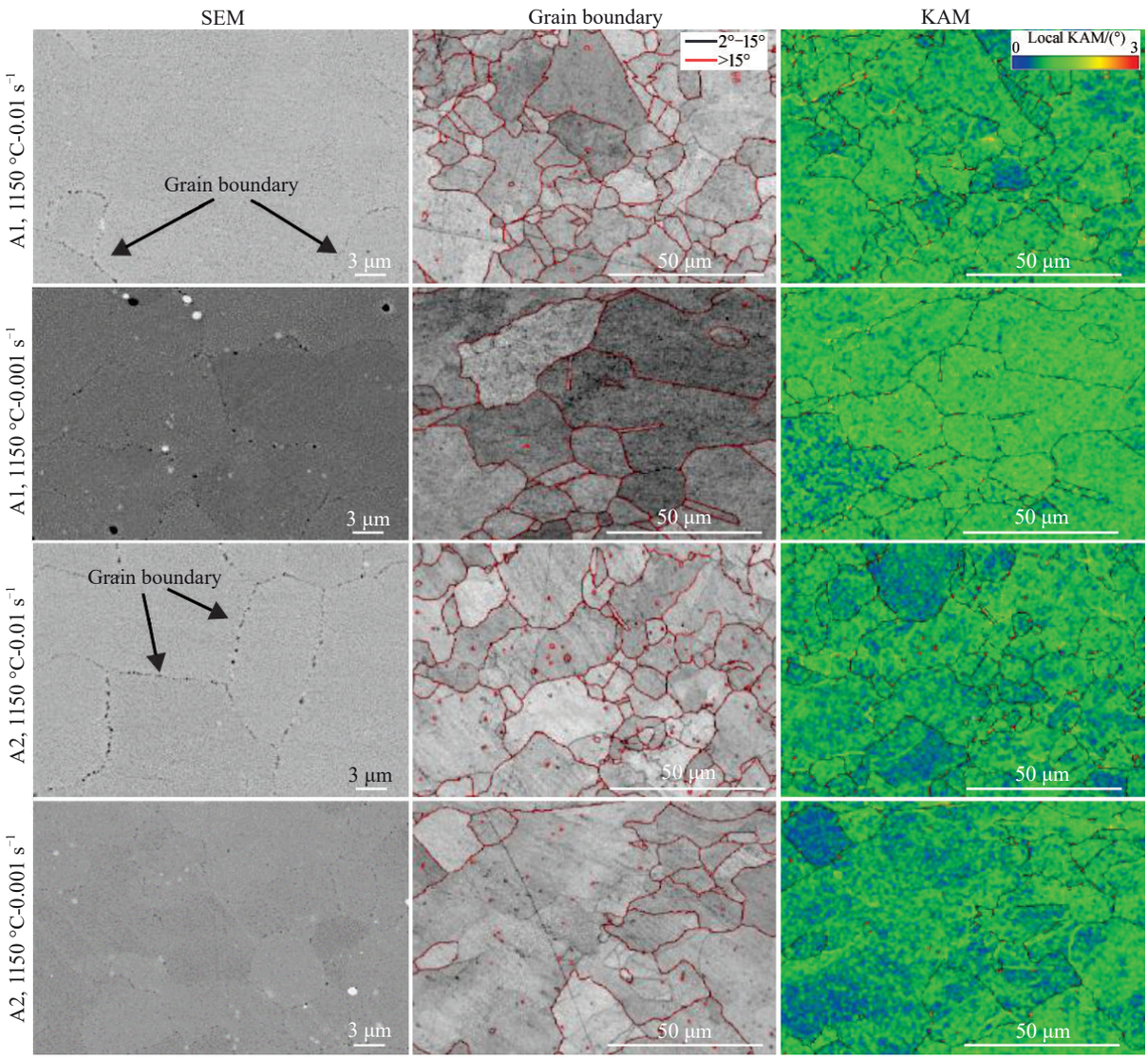

Fig.6 SEM image, grain boundary, and KAM distribution of samples after hot deformation at 1150 °C with different strain rates

undergo secondary work-hardening and recrystallizing again in A2 sample. When deformed at high temperature, the γ' phases are dissolved and the pinning effect decreases. Meanwhile, dislocations, sub-grain boundary and grain boundary migration rates are faster and RX is accelerated. The flow stress curve shows a uniform upward trend, because the RX grain grows up during the deformation at high temperature and low strain rate, which weakens the grain boundary coordination mechanism and significantly increases the resistance[16,33,35]. The deformation resistance of extruded ultrafine microstructure (A2) is slightly greater than that of extruded fine microstructure (A1).

The RX behavior of FGH4113A superalloy is sensitive to the deformation temperature. Summarily, the GOS, KAM, and grain size of FGH4113A superalloy are dramatically affected by the initial microstructure, the deformation temperature, and strain rate.

TEM images of samples under different deformation conditions are depicted in Fig. 8. For the A1 sample deformed at 1050 °C -0.01 s^{-1}, sub-grain microstructures formed by dislocation accumulation in the deformed grains, recrystallized grains, twins (Fig. 8a), and entangled deformation dislocations (Fig. 8b) can be observed. Massive substructure and dense dislocation wall lead to an increase in the stored energy in the material. The stacked dislocations accelerate the dissolution of γ' phase. When the stored energy is sufficient to overcome the boundary curvature, the sub-grains can bulge into the matrix as a new grain. Strain-induced boundary migration becomes RX nucleation mechanism[23,32,38].

When deformed at 1100 °C, coexistence of recrystallized grains and deformed grains are observed in A2 sample. γ' phases can be seen both in the grains and at grain boundaries, where they restrict grain boundary migration[35,39]. The sample deformed at 1150 °C -0.01 s^{-1} consists of coarse grains with straight grain boundaries, indicating complete RX, while some dislocations are observed within the grains. The dislocations in TEM image confirm the secondary work hardening behavior in A2 sample.

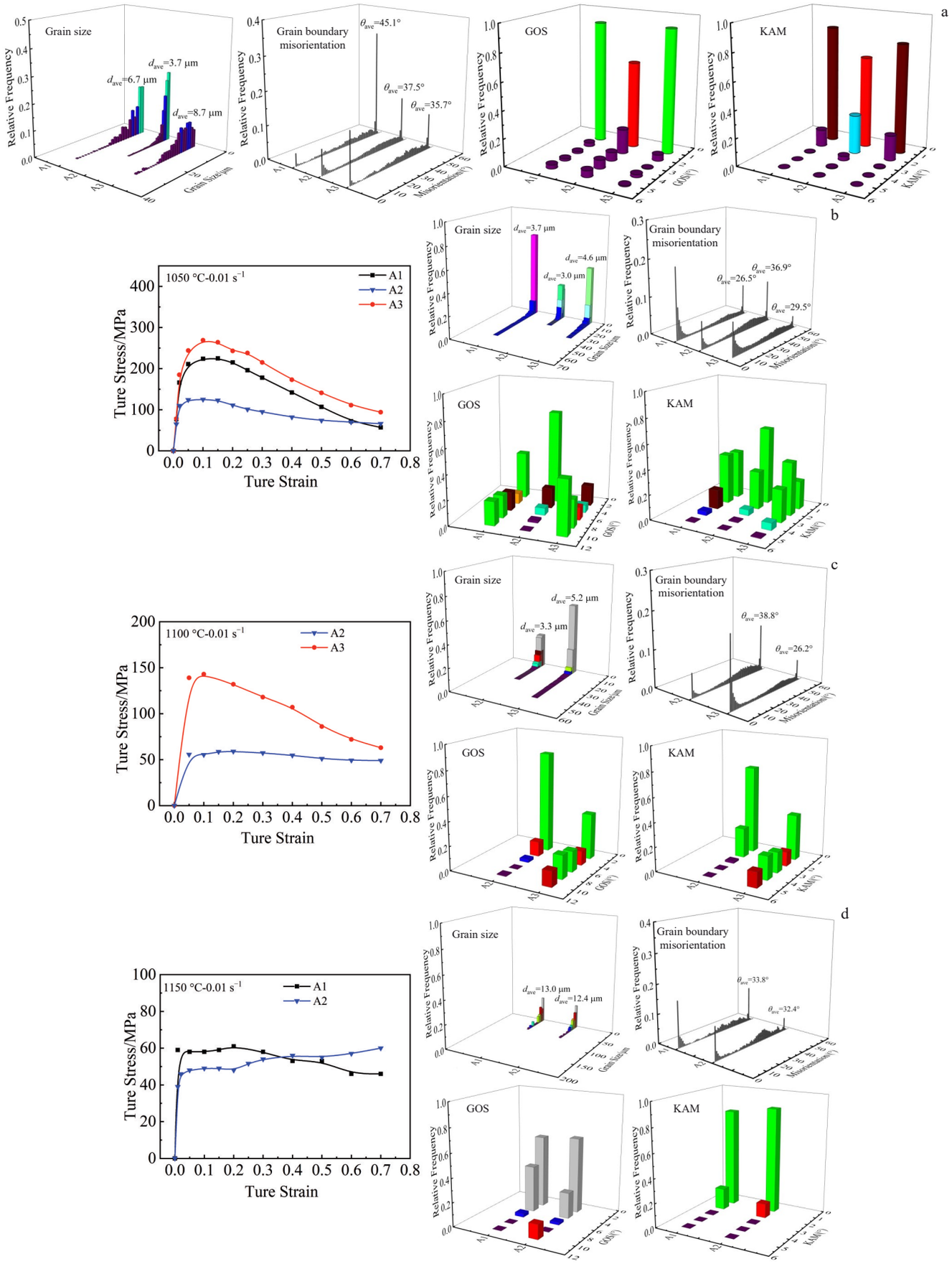

Fig.7 Grain size, grain boundary misorientation, GOS, and KAM distribution of samples after hot deformation under different conditions: (a) as-received, (b) 1050 °C-0.01 s^{-1}, (c) 1100 °C-0.01 s^{-1}, and (d) 1150 °C-0.01 s^{-1}

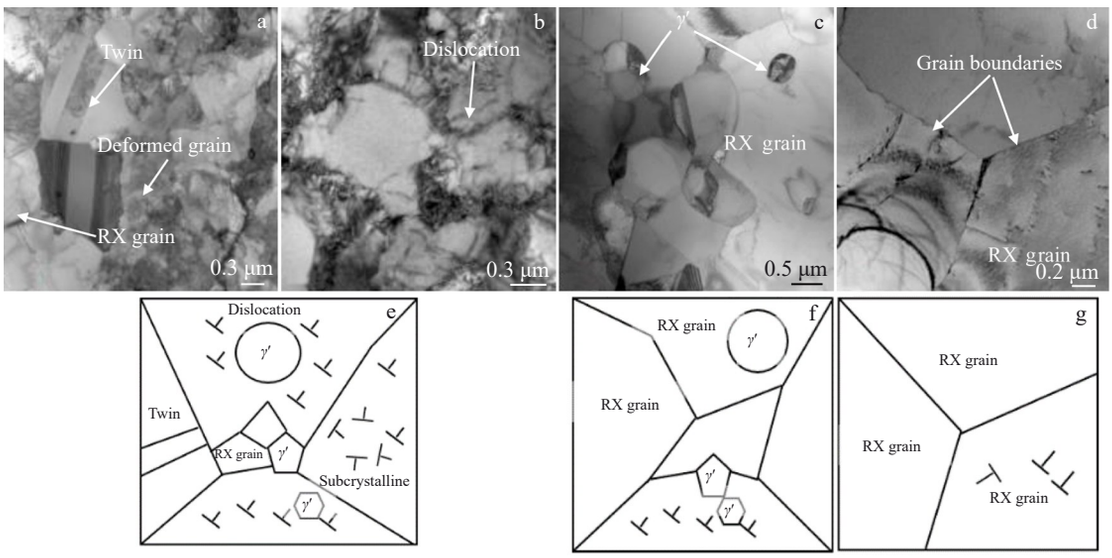

Fig.8 TEM images and corresponding schematic diagrams of samples under different deformation conditions: (a–b, e) A1, 1050 ℃-0.01 s^{-1}; (c, f) A2, 1100 ℃-0.01 s^{-1}; (d, g) A2, 1150 ℃-0.01 s^{-1}

4 Conclusions

1) The A1 sample consists mainly of PPB and γ' phase. The A2 sample displays a $\gamma + \gamma'$ duplex microstructure with uniformly distributed fine grains. The A3 sample exhibits a heterogeneous microstructure characterized by non-uniform grain sizes and the presence of residual γ' phase. All three samples, A1, A2, and A3, demonstrate complete recrystallization, with distinct average grain sizes of 6.7, 3.7, and 8.7 μm, respectively.

2) When deformed at 1050 and 1100 ℃, a fine-grained microstructure (A2) is beneficial for RX during the hot deformation process. The A2 sample exhibits complete RX, and its stress-strain curve is in a hardening-softening equilibrium state. In contrast, A1 and A3 samples display a necklace-like microstructure, corresponding to the softening region of the true stress-true strain curve. In the deformed A1 sample, dislocation tangles, sub-grains, twins, and recrystallized grains can be observed.

3) During deformation at 1150 ℃, the deformation behavior and microstructure of the A1 and A2 samples with different microstructures are similar, with average grain sizes of 13.0 and 12.4 μm, respectively.

References

1 Reed R C, Rae C M F. *22 - Physical Metallurgy of the Nickel-Based Superalloys, Physical Metallurgy (Fifth Edition)*[M]. Elsevier: Oxford, 2014: 2215

2 Atkinson H V, Davies S. *Metallurgical and Materials Transactions A*[J], 2000, 31(12): 2981

3 Qiu C L, Attallah M M, Wu X H *et al. Materials Science and Engineering A*[J], 2013, 564: 176

4 Bai Q, Lin J, Tian G *et al. Journal of Powder Metallurgy and Mining*[J], 2015, 4(1): 127

5 Xiao Lei, He Yingjie, Ma Xiangdong *et al. Rare Metal Materials and Engineering*[J], 2022, 51(6): 2215 (in Chinese)

6 Wen H N, Tang X, Jin J S *et al. Materials Science and Engineering A*[J], 2022, 847: 143356

7 Tan L M, Li Y P, Liu C Z *et al. Materials Characterization*[J], 2018, 140: 30

8 Liu Y H, Ning Y Q, Yang X M *et al. Materials & Design*[J], 2016, 95: 669

9 Ning Y Q, Yao Z K, Fu M W *et al. Materials Science and Engineering A*[J], 2010, 527(26): 6968

10 Liu W, Liu Z L, Zhang H *et al. Journal of Alloys and Compounds*[J], 2023, 938: 168574

11 Ning Y Q, Yao Z K, Yang Z *et al. Materials Science and Engineering A*[J], 2012, 531: 91

12 Liu T, Cheng X, N Ding H N *et al. Materials Science and Engineering A*[J], 2023, 871: 144922

13 Kumar S S, Raghu T, Bhattacharjee P P *et al. Materials Characterization*[J], 2018, 146: 217

14 Li F L, Fu R, Yin F J *et al. Journal of Alloys and Compounds*[J], 2017, 693: 1076

15 Ning Y Q, Yao Z K, Guo H Z *et al. Materials Science and Engineering A*[J], 2010, 527(26): 6794

16 Li Fulin, Fu Rui, Bai Yunrui *et al. Acta Metallurgica Sinica*[J], 2023, 59(7): 855 (in Chinese)

17 Wu H, Liu M X, Wang Y *et al. Journal of Materials Research and Technology*[J], 2020, 9(3): 5090

18 Zhang C, Zhang L W, Li M F *et al. Journal of Materials Research*[J], 2014, 29(23): 2799

19 Xie B C, Ning Y Q, Zhou C. *Procedia Engineering*[J], 2017, 207: 1093

20 Wan Z P, Hu L X, Sun Y *et al. Vacuum*[J], 2018, 155: 585

21 Chen J Y, Dong J X, Zhang M C *et al. Materials Science and*

Engineering A[J], 2016, 673: 122
22 Liu F F, Chen J Y, Dong J X *et al. Materials Science and Engineering A*[J], 2016, 651: 102
23 Jia D, Sun W R, Xu D S *et al. Journal of Alloys and Compounds*[J], 2019, 787: 196
24 Liu P, Zhang R, Yuan Y *et al. Journal of Alloys and Compounds*[J], 2020, 831: 154618
25 Wang J W, Chen Y B, Zhu Q *et al. Acta Metallurgica Sinica*[J], 2022, 58(6): 726
26 Alniak M O, Bedir F. *Materials Science and Engineering B*[J], 2006, 130(1): 254
27 Gabb T P, Gayda J, Falsey J. *Forging of Advanced Disk Alloy LSHR*[R]. Ohio: Glenn Research Center, 2005
28 Yang Q M, Lin Y C, Liu G *et al. Journal of Alloys and Compounds*[J], 2023, 947: 169653
29 Yang Q M, Lin Y C, Zhao W W *et al. Journal of Materials Research and Technology*[J], 2023, 27(11): 9037
30 Ning Y Q, Yao Z K, Yue T W *et al. Rare Metal Materials and Engineering* [J], 2009, 38(10): 1783
31 Yang Q M, Lin Y C, Chen M S *et al. Materials*[J], 2022, 15: 4030
32 Cram D G, Zurob H S, Brechet Y J M *et al. Acta Materialia*[J], 2009, 57(17): 5218
33 Wang C Y, Song X J, Zou J W *et al. Hot Working Technology*[J], 2019, 48(11): 39
34 Dehghan-Manshadi A, Hodgson P D. Metallurgical H J *et al. Metallurgical and Materials Transactions A*[J], 2008, 39: 2830
35 Zhang W W , Liu X, Du Q *et al. Journal of Materials Research and Technology*[J], 2023, 23: 13
36 Tan L M, Li Y P, He G A *et al. Materials Characterization*[J], 2019, 147: 340
37 Qin F M, Zhu H, Wang Z X *et al. Materials Science and Engineering A*[J], 2017, 684: 634
38 Zurob H S, Bréchet Y, Dunlop J. *Acta Materialia*[J], 2006, 54(15): 3983
39 Song K, Aindow M G. *Materials Science and Engineering A*[J], 2008, 479(1): 365

显微组织对FGH4113A高温合金热变形行为和组织演变的影响

杨金龙[1,2]，熊江英[2,3]，尹　超[3]，程俊义[2,3]，郭建政[2,3]，冯赣江[2,3]
(1. 深圳市万泽航空科技有限责任公司，广东 深圳 518000)
(2. 中南大学 粉末冶金研究院，湖南 长沙 410083)
(3. 深圳市万泽中南研究院有限公司，广东 深圳 518000)

摘　要：研究了热等静压（HIP，A1）、热等静压+1100 ℃热挤压（A2）、热等静压+1150 ℃热挤压（A3）3种不同热变形条件下的热压缩曲线和变形组织。结果表明：1100 ℃挤压的A2样品具有均匀的$\gamma+\gamma'$双相细晶粒组织，1050和1100 ℃条件下均表现出良好的热变形性能。在较大应变范围内，A2样品的真应力-真应变曲线保持了硬化-软化平衡状态，变形后平均晶粒尺寸5 μm。热等静压态A1样品和1150 ℃挤压A3样品在1050 ℃仍处于变形软化阶段，组织为原始粗大晶粒和细小再结晶晶粒的混合项链晶，样品的再结晶形核机制主要为应变诱发晶界弓弯形核。1150 ℃–0.001 s^{-1}条件下，初始组织对热变形行为和变形后组织的影响相对较小，变形后组织为完全再结晶的晶粒。细晶组织有利于最大化合金的热变形潜力。通过合理地调控变形机制，可以获得细小均匀的变形组织。

关键词：FGH4113A高温合金；初始显微组织；热变形行为；组织演变

作者简介：杨金龙，男，1988年生，博士，高级工程师，深圳市万泽航空科技有限责任公司，广东 深圳 518000，电话：0755-82799834，E-mail：yangjinlong0419@csu.edu.cn